

The Morphology Dependence of Luminosity Segregation in the Coma Cluster

Nobunari Kashikawa and Maki Sekiguchi¹

Optical and Infrared Astronomy Division, National Astronomical Observatory of Japan, Mitaka,
Tokyo 181, Japan

and

Mamoru Doi, Yutaka Komiyama, Sadanori Okamura, Kazuhiro Shimasaku, Masafumi Yagi, and
Naoki Yasuda

School of Science, University of Tokyo, Bunkyo-ku, Tokyo 113, Japan

ABSTRACT

We carry out CCD photometry of galaxies in the 5.25 square region centered on Coma cluster down to $M_R = -16.0$, beyond the limit of conventional morphological classification. We use the angular two-point correlation function as well as radial profiles in order to characterize the luminosity segregation. We find strong luminosity segregation for our total sample over the magnitude range of $-20 \leq M_R \leq -16$, which is not entirely accounted for in terms of the morphology-density relation that is known to exist only for bright galaxies. We use a single consistent parameter, the degree of luminosity concentration, to parameterize the morphology of galaxies over the wide magnitude range, where both giant and dwarf galaxies are included. Galaxies with high central concentration (HCC) show strong luminosity segregation, *i.e.*, their clustering strength depends strongly on luminosity while those with low central concentration (LCC) show almost no luminosity segregation. Radial density profile shows that brighter HCC-type galaxies tend to more strongly concentrate near the cluster center while LCC-type galaxies do not show such a dependence on luminosity. We show that these results are tenable against the contamination by field galaxies and uncertainties in our method of classification.

Subject headings: galaxies: clusters: individual — Coma cluster, galaxies: clustering

1. INTRODUCTION

Some studies suggest that luminous galaxies are clustered more strongly than faint galaxies. This phenomenon is referred to as the luminosity segregation (hereafter LS). The LS can be

¹Present address: Institute for Cosmic Ray Research, University of Tokyo, Tanashi, Tokyo 188

interpreted as a result of either primordial effects or environmental effects. Explanations based on the primordial effect include the biased Cold Dark Matter (CDM) model in which galaxies form at high peaks in the density field (e.g., Kaiser 1984; Davis et al. 1985). It is known that the LS is naturally predicted by this model. Valls-Gabaud, Alimi, & Blanchard (1989) pointed out that the correlation strength has a positive dependence on galaxy luminosity on the basis of the biased-CDM model. White et al. (1987) also predicted that clustering strength is a strong function of the circular velocity of galaxies, which in turn correlates with the luminosity as indicated by Tully-Fisher or Faber-Jackson relations. In terms of environmental effects, the LS can be regarded as a result of frequent merging or other dynamical mechanisms in the vicinity of the cluster core.

Observational evidence for the LS has been uncertain and controversial. Some found positive results (e.g., Capelato et al. 1980; Domínguez-Tenreiro & Pozo-Sanz 1988; Davis et al. 1988), and others found negative results (e.g., Phillips & Shanks 1987; Einasto 1991). The clustering property of galaxies is also correlated with their morphology, which is so-called the morphology segregation, or morphology-density relation (Dressler 1980b). If the morphology segregation is the fundamental correlation, the LS would be naturally expected. Early-type galaxies show a stronger degree of clustering than late-type galaxies, and at the same time, early-type galaxies are on the average brighter than late-type galaxies (e.g., Efstathiou, Ellis, & Peterson 1988). Consequently, galaxies which are more strongly clustered are brighter than those which are less clustered, which is the LS. On the contrary, if the LS is an essential correlation, the morphology segregation would also be expected. Accordingly, it is critical to see if the LS is observed *within a given morphological type* in order to disentangle the coupling of the LS and morphology segregation. Only a few such studies have been made so far (Einasto 1991; Loveday et al. 1995).

There are also few studies on the LS among dwarf galaxies. Binggeli, Tammann, & Sandage (1987) found in the Virgo cluster that nucleated dwarf ellipticals (dEs) are more strongly concentrated towards the cluster center than nonnucleated dEs. Ferguson & Sandage (1989) found in the Virgo and Fornax clusters that the faint ($M_B > -13.3$) nonnucleated dEs have the distribution identical to that of the E/S0 galaxies and bright nucleated dEs. They also found that the faint nonnucleated dEs are more strongly concentrated on the cluster center than the bright nonnucleated dEs. Thompson & Gregory (1993) showed in the Coma cluster that both dEs and dwarf spheroidals have the same distributions as that of giant early-type galaxies. Morphological classifications of these studies are based on the eye inspection and Thompson & Gregory’s criteria used for Coma dwarfs are slightly different from those of Sandage and collaborators used for Virgo dwarfs.

One of the reasons why the LS has not been examined systematically is the difficulty in sampling a large number of faint galaxies with known absolute magnitude. Clusters of galaxies are good targets to address the problem of the LS in high density environments. In particular, in nearby clusters we can sample intrinsically faint galaxies, which are critically important to the study of the LS. However, nearby clusters have such a large apparent size that we cannot survey whole the cluster with a CCD which has a small physical size.

In this study, we present the angular two-point correlation function as well as the radial profiles of galaxies in the Coma cluster on the basis of a large homogeneous sample covering a wide magnitude range $-20 \leq M_R \leq -16$, where both giant and dwarf galaxies are included. We examine if there is a difference in these properties between the galaxies which have high central concentration of the surface brightness distribution and those with low central concentration. Our sample is made available by three new techniques; CCD mosaic, semi-automated data reduction/analysis software, and quantitative and objective classification of morphological type of galaxies based on surface photometry parameters.

In section 2, we briefly explain our imaging observation of the Coma cluster. In section 3, we describe the data reduction procedures, calibration methods which are special to our camera, and the method of constructing a homogeneous galaxy sample. In section 4, we describe star-galaxy discrimination, evaluation of the number of contaminated field galaxies, and the method of classifying galaxies according to the surface brightness concentration. We present our results in section 5. Finally, reliability of our results is discussed in section 6 in terms of the effects of uncertainties in our classification and contamination by background galaxies. A comparison with previous studies are given in section 7.

2. OBSERVATIONS

We observed the Coma cluster region on May 1–2, 1992 and March 17–21, 1993 with our mosaic CCD camera (hereafter M CCD1) mounted on the prime focus of the Kiso 105cm Schmidt telescope. M CCD1 consists of an 8×2 array of 1000×1018 -pixel CCDs. CCDs are placed with a relatively large space between the chips (Figure 1). One contiguous field is completed by taking several exposures, each shifted by a fixed amount on the CCD grid. A technical description of M CCD1 is presented in Sekiguchi et al. (1992).

The image scale at the Kiso Schmidt prime focus is $0.''75/\text{pixel}$. The sky coverage is $1.^{\circ}7 \times 3.^{\circ}4 = 5.25$ square degrees and the center of the surveyed region is ($12^h 59^m 35.^s2$, $+27^{\circ} 57' 35''$) (J2000.0). One exposure of our camera is referred to as a ‘shot’, which produces 16 frames for M CCD1. We have to take 15 shots for M CCD1 to complete the survey of one contiguous field. A contiguous image consists of about 16250×8100 pixels constructed from $16 \times 15 = 240$ frames. One CCD chip was dead, and thus the data are lacking in the southwest corner (~ 0.35 square degrees). We obtained 225 frames (15 chips times 15 shots) of a 20 minutes exposure in the R band. The seeing size was $3.''8$ FWHM on average.

3. DATA REDUCTION PROCEDURES

The data produced by our mosaic CCD camera amount to about 1 to 3 GB per night. We have developed a suit of software which reduces these large amount of data. Details of this

software package will be given by Yagi et al. (1998). The best performance of the package is attained by two-pass processing. The first pass is to fine-tune several critical parameters that are used in the second pass, which produces the final catalog of objects with photometric parameters together with parameters necessary to construct one contiguous image.

Functions of our software package contain (1) flat fielding, (2) sky subtraction, (3) bright objects detection, (4) mosaicking, (5) smoothing, (6) objects detection and parameterization, (7) photometric calibration, (8) astrometric calibration, (9) star/galaxy discrimination, and (10) morphological classification. The tasks (1)-(6) are carried out ‘on-line’, *i.e.*, in a semi-automatic routine basis while tasks (7)-(10) are performed ‘off-line’. Tasks (1)-(8) are briefly explained below and tasks (9) and (10) are described in section 4.

3.1. Flat Fielding and Sky Subtraction

In flat fielding, each frame is reduced according to the ordinary way of CCD data reduction. The sky-flat frame for each chip is constructed by taking the median value for each pixel of a lot of object frames (15 – 20 frames) exposed with the chip at different sky regions. We also construct the median dome-flat frame as well as the sky-flat frame. The flat frame is constructed by multiplying the sky-flat frame with the dome-flat frame and normalizing the resultant frame so that the average count of all the pixels becomes unity. Bias subtraction and flat fielding, *i.e.*, dividing by the flat frame, are carried out independently for each CCD chip. Dark current was negligible and no fringe or interferometric pattern was seen in our data.

We subtract the sky-background count from the flat fielded frames. The local sky background is computed as follows. First, we divide each frame into 10×10 meshes, each consisting of 100×100 pixels. A histogram of pixel counts is constructed for every mesh. The peak of the histogram is determined by fitting a Gaussian to the low count side of the histogram and the count at the peak of the Gaussian is regarded as the representative sky count for the mesh. The representative sky counts are assigned to the central pixels of respective meshes. A bi-linear interpolation of those representative counts is performed to determine the local background sky count of every pixel in the frame, which is subtracted from the pixel count of the flat fielded frame.

3.2. Coarse Finding of Bright Stars

Before we detect objects and measure their photometric parameters, the coarse detection is done to find some parameters for constructing a homogeneous sample all over the survey field. Our object finding is based on the so-called ‘connected pixel method’. We recognize a lump of pixels whose counts are above a threshold value, I_{th} , as an object when it consists of more pixels than a minimum number, N_{min} . We empirically set the minimum number to the number of pixels enclosed within the circle with a diameter of the FWHM of the seeing size, and the threshold

value to be several times of sky r.m.s. fluctuations above the sky. The detected objects in this procedure are used for seeing measurement and mosaicking which will be explained below.

3.3. Seeing Measurement

In each frame, images of typical stars are scissored out and shifted so that the centers of gravity of the stellar images are coincident. Then, all the images are added together to give a combined stellar image. We measure the seeing size by fitting a Gaussian to the central region of the combined stellar image. We take the FWHM of the Gaussian as the seeing size. The seeing size of frames exposed on different chips should be, in principle, identical for the same exposure. We find a small change in the seeing size for different frames even within the same exposure. This may be due to the slight tilt of the dewar mount with respect to the optical axis. A tiny distortion of the image caused by guide errors is also found in this combined stellar image. In this paper, we refer the ‘seeing size’ to the FWHM size of the Gaussian fitted to this combined stellar image.

3.4. Smoothing

Now we have obtained the seeing size for all the frames. The difference in the seeing size among different exposures, if significant, should be corrected for by smoothing the data at least to the first order approximation. The frames with smaller seeing sizes should be smoothed with a Gaussian beam so that all the frames for a contiguous field have the same seeing size. This seeing equalization procedure is important to obtain a homogeneous photometric sample over the field because we derive isophotal magnitudes and sizes which are affected easily by seeing, especially, in case of faint galaxies (Yoshii 1993).

We finally adjust seeing size at $\sim 4.''5$. In spite of the seeing equalization, there is a little residual tendency that the chips on south-side (larger number in each row) show larger FWHM. This is supposed to be due to an asymmetric distortion of star images caused by a slight tilt of dewar mounting.

3.5. Mosaicking

The most important process, that is, the frame mosaicking, is attained on the basis of the position and the flux of the stars in the overlapped region between adjacent frames. This process is important because our goal is to obtain a statistically homogeneous sample of galaxies over a wide area detected by the same criteria and measured in the same manner using a mosaicked image which consists of a lot of frames taken at different nights and under different observational conditions.

In the first step of this procedure, triangles of stars are constructed in the overlapped region. A triangle is composed of three stars. Triangles are made for all possible combinations of three stars extracted from the detected stars in the overlapped region. Every triangle on a frame is paired with the corresponding triangle on the adjacent frame to be mosaicked. A pair of the same stars in the two frames is identified by this triangle pattern-matching algorithm (Groth 1986). We determined the size of the overlapped region on the basis of the star count at the north galactic pole (Bahcall & Soneira 1983, hereafter BS83) so that enough stars are included. In fact, at least three pairs of stars were obtained in any overlapped region. In the second step, adjacent frames are shifted, rotated and flux-scaled as follows so that the position and the flux of these star pairs coincide with each other in both frames. The algorithm used in this process is contrived so that the errors in position and flux are evenly distributed over the whole set of frames. We determine four parameters necessary to the mosaicking, *i.e.*, x, y positions, rotation angle, and flux scaling factor of each frame by minimizing the r.m.s. error over the whole set of frames under the restriction that the cumulative sum over any possible loops involving neighboring 2×2 frames would be zero (see Yagi et al. 1998).

The mosaicking error becomes larger as magnitude goes fainter. The r.m.s. of mosaicking errors in positions is estimated to be 0.17 and 0.21 pixels in the magnitude range $17.5 < R \leq 18.0$ for x and y, respectively. The r.m.s. of mosaicking errors in magnitude at the faintest bin $17.5 < R \leq 18.0$ is 0.08mag.

3.6. Finding Objects and Parameterization

Finally the software package outputs a catalog including all the detected objects. We determined the threshold level I_{th} to be 1.5 times the largest sky r.m.s. noise among the frames. The minimum number N_{min} was determined to the number of pixels within the circle with a diameter of the equalized seeing size (FWHM). In this study, I_{th} corresponds to 24.23 mag/arcsec² and N_{min} to 30 pixels. We detect objects and measure several photometric parameters simultaneously. For example, the important parameters we measure are; cx, cy: image centroids (in units of pixels), f_{iso} : total flux above the threshold isophotal surface brightness, N_{pix} : number of connected pixels, I_{peak} : counts at the peak brightness, SB : mean surface brightness, q : axis ratio, p : position angle, C_{in} : central concentration index, and flag for blended objects. C_{in} is defined as

$$C_{in} \equiv \frac{\int_0^{\alpha r(\mu_L)} rI(r)dr}{\int_0^{r(\mu_L)} rI(r)dr}, \quad (1)$$

where $r(\mu_L)$ is the ‘equivalent radius’² at a limiting surface brightness μ_L , and α is a constant ($0 < \alpha < 1$). We take $\alpha = 0.3$ following Doi et al. (1995). Both the axis ratio q and the position angle p are measured on the basis of the profile within the isophote at I_{th} . An object is identified as blended, if it has multiple peaks associated with more than $N_{pix}/10$ pixels when it is sliced step by step toward higher isophotal threshold levels. Objects that are flagged as blended are not included in the sample in this study. The parameter f_{iso} gives the isophotal magnitude (section 3.7), I_{peak} and N_{pix} are used in the star/galaxy discrimination (section 4.1), and C_{in} and SB are used in morphological type classification (section 4.3).

3.7. Photometric Calibration

Photometric zero-point calibration is carried out as an off-line process using photometry of standard stars. We observed standard stars in the globular cluster NGC6205 (Forbes & Dawson 1986). Its size was smaller than the field of view of one CCD chip. Therefore in this calibration, we are concerned with the data taken by a single chip with which we observed standard stars. Since we have a consistent flux scale all over the contiguous field by mosaicking, the zero point of the chip applies to all the field. Proper correction for atmospheric extinction requires the color of galaxies. However, since we have R -band data only, we assume $(V - R) = 0.77$ for all the galaxies we detected. The value 0.77 is the weighted mean of the colors of local galaxies of various morphological types (Yoshii & Takahara 1988). The lack of a color term would make a relatively large photometric uncertainty. We adopt magnitude correction $A_R^b = 0.03$ for Galactic absorption according to Burstein & Heiles (1984), which is based on the HI column density.

3.8. Astrometric Calibration

The Guide Star Catalog (Lasker et al. 1990, hereafter GSC) is used as a reference to transform positions of objects given by the internal coordinates to the celestial coordinates. GSC contains the positions (J2000.0 epoch) of 1.7×10^7 stars all over the sky and the accuracy is claimed to be in the range 0."2 to 0."8 all over the catalog. Common stars cataloged both in our sample and in GSC are found by cross-matching. We have 355 common stars which are almost uniformly distributed in our field. The saturated stars are excluded. The stars we use for reference have errors 0."3 to 0."5, which are sufficiently accurate for our purposes. The standard coordinates (ξ, η) of the reference stars are expressed by the 2nd-order polynomials of the measured (x, y) coordinates, and the plate constants were determined by the least squares method. In the fitting procedure, stars with large residuals are rejected. We use 260 stars for the final fitting. Then (ξ, η) is transformed to (α, δ) . After the transformation, no systematic trend is seen in the residual

²Abraham et al. (1994) proposed a modified scheme using elliptical apertures based on the second moment of images, which is in fact practically identical to our scheme described by Doi et al. (1993).

vectors, except that large ($< 3.''5$) residuals are seen near the southeast corner. Since the data are lacking in the southwest corner, the mosaicking procedure of southeast frames is supposed to be less accurate compared with that of other frames. The residual of the fit to the reference stars lies in the range $-2.''5 - 3.''5$ (r.m.s. error is $\sim 1''$). The errors are small enough and do not affect the measurement of the angular correlation function.

4. SAMPLE SELECTION

4.1. Star/Galaxy Discrimination

The catalog of detected objects contains stars, galaxies, cosmic rays, dusts or defects on the CCD chips, and other noises. Our technique for distinguishing galaxies from stars is based on the difference in image profile that the image of a galaxy is more extended than that of a star. The stellar image is determined by the instrumental optics and the seeing, and therefore lies in a well-defined region of an appropriate parameter space.

We take a parameter $\log(I_{peak}/N_{pix})$ as a star/galaxy discriminator where I_{peak} is the peak count of an object image and N_{pix} is the number of connected pixels above a given threshold. Stars are expected to have a higher $\log(I_{peak}/N_{pix})$ than galaxies at the same magnitude. The diagram we use for star/galaxy discrimination is shown in Figure 2. Stars form a well-defined sequence running from top-left to middle-right in Figure 2, while galaxies are distributed extensively below the star sequence indicating that galaxy profiles have more significant variations. The star sequence merges into the galaxy locus at $m_R \sim 18.5$. Faint stars become indistinguishable from galaxies because of seeing and increasing noise. The objects which are distributed above the merged star/galaxy sequence in the faint region ($m_R \geq 19.0$) were confirmed to be defects, noises, or cosmic rays. The star sequence terminates rather abruptly at the bright end ($m_R < 15$). This is due to the fact that we excluded the bright saturated stars. Since some of the brightest galaxies are also excluded due to saturation, our catalog is not complete for the brightest galaxies ($m_R \leq 13.5$).

We define the boundary line between stars and galaxies, which is drawn manually and denoted by the solid line in Figure 2. Then we compare the star counts with those of Yamagata & Yoshii (1992, hereafter YY92) model for the same galactic coordinates as the Coma cluster region. This model is more sophisticated than the model given by BS83. The YY92 model is based on number counts of stars with more precise and deeper observations, and the thick disk component is introduced in the model (Yoshii 1994, private communication). In Figure 3, the observed star counts (filled circle) based on the boundary we define show very good agreement with the YY92 model (solid line), while observed star counts disagree with the BS83 model (dotted line). The faint limit of our galaxy sample extracted with this star/galaxy discrimination method is determined to the magnitude at which our star counts becomes inconsistent with the YY92 model. The faint limit is $m_R \sim 18.5$. This limiting magnitude is largely influenced by the seeing size.

4.2. Estimate of the Number of Field Galaxies

In order to investigate the properties of cluster galaxies, it is necessary to estimate the contamination by background and foreground galaxies, which we call ‘field’ galaxies hereafter. We estimate the number of contaminating field galaxies with our own imaging data for SA57. The center position of the field we surveyed is ($13^h09^m46.^s6$, $+29^\circ23'02''$) (J2000.0), which is $2.^{\circ}65$ away from the Coma center. The data were taken by our second mosaic CCD camera, MCCD2 (Kashikawa et al. 1995a; Okamura et al. 1997) at the prime focus of the William Herschel Telescope in 1996 Apr. MCCD2 is basically the same instrument as MCCD1. The total survey area was 0.44 square degree with $1.''0$ seeing which is much better than those of the Coma data. The SA57 data were smoothed with a Gaussian beam so as to have the seeing size $\sim 4.''5$ of the Coma data. We apply to the SA57 data the same manner of data reduction, the same detection threshold, and the same star/galaxy-separation method as those for the Coma data.

The expected contamination rate, *i.e.*, the number of field galaxies with respect to that of our Coma galaxies is listed in Table 1 as a function of the limiting absolute magnitude. We restrict our sample to galaxies brighter than $m_R^{lim} = 18.21$ ($M_R^{lim} = -16.00 + 5\log h$), where the contamination rate reaches $\sim 50\%$. We here assume the distance modulus of the Coma cluster to be $(m - M)_0 = 34.21$ which is derived from the mean velocity $\bar{v} = 6942\text{kms}^{-1}$ (Zabludoff, Geller, & Huchra, 1993). Throughout this paper we adopt a Hubble constant $H_0 = 100h\text{km/s/Mpc}$. We hereafter use $h = 1$ where the h dependence is not explicitly indicated.

4.3. Morphological Classification

We classify the sample galaxies into two subsamples using a single consistent parameter, the degree of luminosity concentration, to parameterize the morphology of galaxies over the wide magnitude range $-20 \leq M_R \leq -16$, where both giant and dwarf galaxies are included. One consists of galaxies which have high central concentration of surface brightness (hereafter HCC), and the other consists of those with low central concentration (hereafter LCC). As for the giant ($M_R \leq -18$) galaxies, the former generally corresponds to early-type galaxies (Hubble morphological type Elliptical/S0, the type index $T = -6 - -1$) and the latter to late-type galaxies (Spiral, $T = 1 - 10$). This method performs a crude classification using the known properties of giant galaxies that early-type galaxies show de Vaucouleurs’ surface-brightness profile which has higher central concentration (corresponds to larger C_{in} in our measured parameters, see section 3.2) than the exponential profile of late-type galaxies. The basic idea of this method is described in Okamura, Kodaira, & Watanabe (1984) and extended by Doi, Fukugita, & Okamura (1993) who used the parameters C_{in} and SB to classify galaxy morphology. They showed that the method is robust for a variety of image size and inclination of galaxies. Note that both of these parameters are distance independent.

As for the morphological classification of dwarf galaxies ($M_R > -18$), on the other hand,

there is no generally accepted quantitative definition, which sometimes leads to confusion (e.g., Ferguson & Binggeli 1994). In this study, we classify both giant and dwarf galaxies on the basis of the single objective photometric parameter C_{in} . However, we extrapolate the critical line between the bright HCC and the bright LCC galaxies to dwarf galaxies as described below. Readers should be careful that the HCC/LCC dwarfs do not correspond to so-called ‘early-type dwarfs’/ ‘late-type dwarfs’. It might be more relevant to suppose that the faint HCC corresponds to the ‘nucleated dE’, and the faint LCC to the ‘non-nucleated dE’, ‘dS0’, and ‘dwarf spheroidals’. However, it is unclear at the moment what our HCC/LCC dwarfs actually mean in terms of these morphological types which are based on the eye inspection. A similar analysis of, for example, the Virgo dwarfs using high-resolution imaging data would be useful to understand this.

In practice, we compute C_{in} for two series of model galaxies with different magnitudes, surface brightness, and axis ratios; one is for galaxies with de Vaucouleurs’ law profile (C_{in}^E) and the other for galaxies with the exponential law (C_{in}^S). The parameter ranges are taken so that they cover those of our sample galaxies, *i.e.*, $14.0 \leq m_R \leq 20.0$, $21.0 \leq SB \leq 24.0$, and $0.2 \leq \text{axis ratio} \leq 1.0$. The model galaxies are smeared with the seeing profile (a single Gaussian) with our observed seeing size ($\sim 4.''5$). We obtain the model-predicted C_{in} for de Vaucouleurs’ law profile and the exponential law profile for each sample galaxy by ‘measuring’ the model profile with the same threshold as for the real sample.

In the Coma cluster sample, we identify some bright galaxies whose morphological types are given in Dressler (1980a). These bright galaxies are shown in Figure 4 in the C_{in} versus magnitude space as well as the locus of the two series of the models. It is found that the model prediction is consistent with Dressler’s classification.

With the model galaxies, we define for each sample galaxy the critical value C_{in}^{crit} by which we classify it either into the HCC type or into the LCC type as

$$C_{in}^{crit} = C_{in}^S + p \times (C_{in}^E - C_{in}^S), \quad (2)$$

where p is a free parameter, and C_{in}^E and C_{in}^S are the values of C_{in} of model galaxies with de Vaucouleurs’ law profile and the exponential profile, respectively, that have the same magnitude, same surface brightness, same seeing size, and same axis ratio as the sample galaxy. We classify a galaxy as the HCC/LCC type when it has C_{in} larger/smaller than C_{in}^{crit} . We determine the parameter p empirically as follows using the Dressler’s classification as fiducial. We investigate the completeness of the subsamples by changing p from 0.0 to 1.0. Here we define the completeness of the sample $C_e(p)$ for early types and $C_s(p)$ for late types as

$$C_e(p) = \frac{N_{ee}}{N_{ee} + N_{se}}, \quad \text{and} \quad C_s(p) = \frac{N_{ss}}{N_{ss} + N_{es}}, \quad (3)$$

respectively, where N_{ee} is the number of Dressler’s early-type galaxies classified correctly as

the HCC type at given p , N_{se} Dressler’s late-type galaxies mis-classified as the HCC type, N_{ss} Dressler’s late-type galaxies classified correctly as the LCC type, and N_{es} of Dressler’s early-type galaxies mis-classified as the LCC type. Both $C_e(p)$ and $C_s(p)$ are shown in Figure 5 as a function of p . The completeness of early-type sample $C_e(p)$ decreases with p , while $C_s(p)$ increases with p . Both C_e and C_s change smoothly with p and are well determined regardless of the magnitude. To obtain an impartial sample for both early-type and late-type galaxies, we choose p that makes $C_e(p)$ equal to $C_s(p)$ as the ‘standard’ value. The standard p is chosen to be 0.35 (Figure 5). We call this sample with $p = 0.35$ as the ‘standard sample’. Figure 6 shows the magnitude versus C_{in} plot for the standard sample. Galaxies classified as the HCC type are indicated by filled circles and those as the LCC type by open circles.

To evaluate the uncertainty in this morphological classification, we make two additional samples; one is the ‘upper sample’ which is made with $p = 0.40$, and the other is the ‘lower sample’ with $p = 0.30$. In the upper sample, we can obtain a higher purity in the sample of the HCC-type galaxies at the cost of lower completeness, while in the lower sample, we obtain a higher purity in the sample of the LCC-type galaxies. The influences of this uncertainty will be discussed in section 6.2.

The sky distribution of galaxies is shown in Figure 7 for the total, HCC, and LCC samples. A larger symbol denotes a brighter galaxy. It is evident that the bright HCC-type galaxies have a more centrally concentrated distribution on the sky which is consistent with the morphology-density relation (Dressler 1980b). This suggests that our classification works well.

Among the three limiting magnitudes, *i.e.*, the limit of star/galaxy discrimination ($M_R = -15.7$), that due to the contamination of the field galaxies ($M_R = -16.0$), and that of morphological classification ($M_R = -15.5$), the brightest limit ($M_R = -16.0$) should determine the limiting magnitude of the final sample for our analysis. The total number of galaxies cataloged is 1822, and morphological contents are 1313 for the HCC and 509 for the LCC. The luminosity function is given in Kashikawa et al. (1995b) together with those of three other nearby clusters.

5. RESULTS

5.1. Luminosity Segregation

5.1.1. Angular Correlation Function

To quantify the galaxy clustering, we use the angular two-point correlation function $\omega(\theta)$, which is usually used for estimating the clustering of field galaxies. Most of previous studies used radial profiles to investigate the clustering properties in rich clusters assuming the symmetric structure of clusters. However, quite a few clusters are known to show asymmetry or substructures and the Coma cluster is no exception (e.g., Briel, Henry & Böhringer 1992; Caldwell et al. 1993).

The $\omega(\theta)$, which quantifies any sort of distributions for different correlation scales, is hardly affected by asymmetry and therefore considered to be a robust measure of clustering properties in clusters as well as fields.

The $\omega(\theta)$ is defined by δP_{12} , the differential probability of finding a pair of galaxies, one in solid angle $\delta\Omega_1$, and the other in $\delta\Omega_2$ separated by θ_{12} :

$$\delta P_{12} = n^2[1 + \omega(\theta_{12})]\delta\Omega_1\delta\Omega_2, \quad (4)$$

where n is the average number density of galaxies (Peebles 1980). In practice, $\omega(\theta)$ is derived by,

$$\omega(\theta) = \frac{N_{gg}(\theta)}{N_{gr}(\theta)} \frac{2N_r}{(N_g - 1)} - 1, \quad (5)$$

where $N_{gg}(\theta)$ is the number of pairs of galaxies separated by θ , $N_{gr}(\theta)$ is the number of pairs of a galaxy and a random point separated by θ as well, N_g is the number of galaxies, N_r is the number of random points. The random points are generated so that they are distributed in the area identical in shape to the area we surveyed. Circular regions around several bright stars, and rectangular regions where pixel defects are present are excluded from the area of the random sample, in the same manner as in the real sample. In each random sample, random points are generated ten times the number of sample galaxies, and $N_{gr}(\theta)$ evaluation is made for twenty different random samples. Therefore, errors caused by the random number generation are negligible.

Our code is first checked with random samples to confirm that $\omega(\theta) \sim 0$ over all scales, and then checked with the CfA sample (de Lapparent, Geller, & Huchra 1988) to make sure that our code reproduces the same $\omega(\theta)$ as they derived.

The $\omega(\theta)$ of field galaxies is well approximated by a power law

$$\omega(\theta) = A_\omega\theta^\gamma. \quad (6)$$

Though it is not sure that this approximation is also adequate for cluster galaxies, we here take the same power law fitting. We can quantify the clustering properties by two parameters, the amplitude A_ω and the power index γ . In addition to A_ω and γ , we introduce a single parameter W_{int} as the integration of $\omega(\theta)$ from θ_1 to θ_2 :

$$W_{int} = \int_{\theta_1}^{\theta_2} \omega(\theta)d\theta. \quad (7)$$

We choose (θ_1, θ_2) as $(0.^\circ 1, 1.^\circ 0)$ corresponding to the physical scale $(0.12h^{-1}\text{Mpc}, 1.20h^{-1}\text{Mpc})$ at the Coma distance.

The sampling error in two point correlation function is usually larger than the error due to Poissonian fluctuation (Mo, Jing, & Börner 1992). The 1σ errors in these parameters A_ω , γ , and W_{int} , and error bars of each bin are estimated by the bootstrap resampling method (hereafter BRM; Diaconis & Efron 1983; Barrow, Bhavsar, & Sonoda 1984).

We extract three subsamples of different absolute magnitudes from the total sample, the HCC sample, and the LCC sample: $M_R \leq -18.0$ (the bright sample), $-18.0 < M_R \leq -17.0$ (the intermediate sample), and $-17.0 < M_R \leq -16.0$ (the faint sample). Since some of the brightest galaxies ($M_R \leq -20.7$) are saturated, we excluded them from the bright sample.

5.1.2. Luminosity Segregation in the Total Sample

Figure 8(a) represents the $\omega(\theta)$ s of the three subsamples extracted from the total sample. The $\omega(\theta)$ s are computed for separations up to the scale at which the amplitude of $\omega(\theta)$ falls to negative. The solid line, the dashed line, and the dotted line indicate the $\omega(\theta)$ for bright sample, intermediate sample, and faint sample, respectively.

Figure 8(a) shows an important result that the amplitude of the $\omega(\theta)$ varies with luminosity. This demonstrates that the degree of clustering shows a pronounced dependence on luminosity of galaxies: brighter galaxies have a much larger correlation amplitude than fainter ones. The parameters, γ , A_ω , W_{int} , and δW_{int} , *i.e.*, the 1σ error in W_{int} estimated by BRM, are listed in Table 2. A systematic trend is found in A_ω and W_{int} that a brighter sample tends to have a larger A_ω and a larger W_{int} . Therefore, the LS is confirmed for the total sample.

The $\omega(\theta)$ s of all the subsamples, especially the bright sample, are flattened at smaller scales ($\theta \leq 0.^\circ 1$), which is consistent with the result obtained by Davis & Geller (1976). They showed that the slope of the $\omega(\theta)$ becomes steeper when galaxies in dense cluster regions are excluded. Brainerd & Villumsen (1992) calculated the spatial two-point correlation function based on N -body simulations of the CDM model and showed that the function becomes flat in high density regions such as clusters of galaxies. The leveling off of the correlation function in the dense cluster region would suggest that clustering properties in rich clusters would be influenced more or less by some non-linear effect of mutual interactions of galaxies or global dynamics in clusters.

5.1.3. Luminosity Segregation in the Morphological Subsamples

We show in Figure 8(b) and in Figure 8(c) the $\omega(\theta)$ s of the three subsamples extracted from the HCC sample and the LCC sample, respectively. For the HCC galaxies, the bright sample has a stronger degree of clustering than the faint sample. The tendency is similar to that seen in

the total sample discussed above. The difference in the clustering amplitude between the bright sample and the faint sample is, however, larger than that found for the total sample. On the other hand, such a tendency can be barely seen for the LCC galaxies (Figure 8[c]). These characteristics are quantitatively seen in the $\omega(\theta)$ parameters listed in Table 2.

Thus, we conclude that the LS is strong in the HCC-type galaxies and weak in the LCC-type galaxies in the Coma cluster. The reason why the LS is observed for the total sample is that $\sim 3/4$ of the total sample is comprised of the HCC type which shows strong LS. In terms of the morphological segregation, Figure 8 and Table 2 clearly demonstrate that galaxies of different morphological types have different clustering properties even in the same range of luminosity.

In addition to the clustering behavior of bright galaxies, we can investigate that of *faint* galaxies ($M_R > -18$) based on the intermediate sample and faint sample. This is a unique feature of the present study. In the intermediate sample, there is no significant difference in the correlation amplitude between HCC and LCC galaxies. On the other hand, HCC galaxies in the faint sample show a slightly weaker correlation amplitude than LCC galaxies in the same sample, though the difference is statistically marginal. Thus, dwarf galaxies do not show as strong morphology segregation as giant galaxies, if the morphology of dwarf galaxies is characterized by the degree of luminosity concentration.

In order to see more clearly the dependence of the clustering strength on limiting magnitude M_R^{lim} , we plot W_{int} as a function of M_R^{lim} in Figure 9. The solid line denotes the HCC-type galaxies and the dotted line denotes the LCC-type galaxies. The error bars show the fluctuations estimated by BRM. The HCC-type galaxies show a strong dependence on the limiting magnitude such that a sample with a brighter limiting magnitude has a larger W_{int} . On the other hand, the W_{int} of the LCC-type galaxies has a weak dependence on the limiting magnitude.

As far as the *bright sample* is concerned, the above findings are qualitatively accounted for by the well-known morphological segregation. The bright HCC-type galaxies are mostly E and S0 galaxies and the bright LCC-type galaxies are mostly spirals. E galaxies stretch to higher luminosity than S0 galaxies. And, E galaxies most favor high density regions, and spiral galaxies least with S0 galaxies in between. These properties explain the larger correlation amplitude of the HCC-type galaxies. The increase in the correlation amplitude of the HCC sample with increasing luminosity can also be accounted for by a larger fraction of E galaxies over S0 galaxies. However, such explanations based on the known properties of bright galaxies are not relevant to the behaviors of the correlation amplitude of the *intermediate and faint samples*.

5.2. Dependence on the Clustercentric Radius

In this section, we examine the properties of galaxies in terms of the cluster structure. Figure 10 shows the surface number density (per square degree) as a function of the radius from the cluster center. Our survey field has a rectangular shape and it includes some rejected regions

with complicated boundaries. We estimate the net area indirectly by counting the artificial random points which are scattered over the effective survey field. We scatter 10^5 random points. We confirm that the counted number of the points for each bin is stable for this random number generation. The cluster center is defined as the position of the midpoint between the two cD galaxies.

The surface number densities of all the subsamples increase toward the cluster center. The bright HCC-type galaxies are strongly concentrated on the cluster center, while the fainter HCC-type galaxies have flatter density profiles. The density profiles of the LCC-type galaxies weakly depend on luminosity. In the faint subsamples, the density profile of the HCC-type galaxies is similar to that of the LCC-type galaxies. If our faint HCC/LCC galaxies correspond to nucleated/non-nucleated dwarfs, this result is different from that found for dEs in Virgo and Fornax clusters (van den Bergh 1986, Binggeli, Tammann & Sandage 1987, Ferguson & Sandage 1989) It is also noted that their samples are restricted to small scales, $\leq 1.4h^{-1}\text{Mpc}$, while ours extends to $\sim 3.0h^{-1}\text{Mpc}$. Quintana (1979) showed that the core radius of the Coma cluster changes significantly with the limiting magnitude of the sample: larger core radii for deeper samples. His finding is consistent with our result. We note, however, that the magnitude dependence of core radius is stronger for the HCC-type galaxies than for the LCC-type galaxies.

6. RELIABILITY OF THE RESULT

6.1. Effects of Contamination by Field Galaxies

As mentioned in section 4.2, our samples are contaminated by non-cluster members, most of which are supposed to be galaxies behind the cluster. The amplitude of $\omega(\theta)$ of a faint sample which contains a larger fraction of field galaxies should be smaller than that of a bright sample including a higher fraction of cluster members because of the following two reasons. One is that field galaxies have an intrinsically weaker clustering amplitude than cluster members. The other is that the amplitude of the $\omega(\theta)$ depends on the effective depth of the sample in such a way that a deeper sample has a weaker amplitude in small scales than a shallower sample, because the same physical length subtends a smaller angle at larger distances, and that more galaxies are seen in projection (Groth & Peebles 1977). The expected contamination rates of field galaxies of our samples are up to 50% (see section 4.2). There remains a possibility that we have mis-classified many field galaxies as HCC types. We undertake the following test to evaluate statistically the effects of field galaxies on our results.

We test whether or not the amplitude difference in $\omega(\theta)$ we observe is caused only by the contamination of field galaxies. As described above, the amplitude of $\omega(\theta)$ depends on the sample depth. The dependence is known to be expressed by a scaling relation of the relativistic version of Limber's equation (Groth & Peebles 1977). It is necessary to include into the scaling relation not only redshift effect and curvature effect but also the effect of luminosity evolution of galaxies when

we are concerned with a deep galaxy sample (e.g., Shanks et al. 1980). In so-called ‘scaling test’, we investigate whether or not the $\omega(\theta)$ s of two samples with different sample depths coincide with each other after one of them is scaled to the other on the basis of the scaling relation. We apply the scaling test to our samples on the assumption that our sample includes some fraction of field galaxies whose sample depth is deeper than that of cluster members.

Consider a sample of galaxies which is composed of cluster members (fraction f_c) and of field galaxies (fraction $f_f = 1 - f_c$). Suppose that cluster members and field galaxies have their intrinsic angular two point correlation functions $\omega_{cc}(\theta)$ and $\omega_{ff}(\theta)$, respectively. The observed $\omega(\theta)$ of the sample is expressed as

$$\omega(\theta) = f_c^2 \omega_{cc}(\theta) + f_f^2 \omega_{ff}(\theta) + 2f_f f_c \omega_{cf}(\theta). \quad (8)$$

We assume no cross-correlation between cluster members and field galaxies, i.e., $\omega_{cf}(\theta) = 0$. We assume that ω_{cc} is independent of the sample depth, i.e., the limiting magnitude of member galaxies in the sample. Therefore ω_{cc} is not subjected to scaling and only ω_{ff} is scaled according to the sample depth. Previous estimates of the $\omega(\theta)$ of field galaxies show that ω_{ff} is approximated by a simple power law as

$$\omega_{ff}(\theta) = A\theta^{-0.8}. \quad (9)$$

The sample depth can be estimated by the galaxy surface number density of the sample (Groth & Peebles 1977). The scaling relation between the amplitude A , which is the amplitude of ω_{ff} at $\theta = 1^\circ$, and the galaxy surface number density, which is a measure of the effective sample depth, was derived by Shanks et al. (1980) for a sample of galaxies in the R band. Their sample, however, covers a deeper magnitude range than our samples and we extrapolate their relation to our brighter magnitude range. The luminosity evolution of galaxies is taken into account in their scaling relation, but it gives no difference in the magnitude range we are concerned.

We construct three new subsamples with different limiting magnitudes, $M_R^{lim} = -18.00$ (16.21 in apparent magnitude), -17.00 (17.21), and -16.00 (18.21), respectively. We estimate the surface number density of galaxies (per square degree), N_{exp} , at the limiting magnitudes of the respective samples with our galaxy counts in the SA57 explained in section 4.2. Then, we derive the predicted amplitude A of each subsample using the extrapolated version of the scaling relation by Shanks et al. (1980). The fraction of field galaxies in each subsample (f_f) is calculated on the basis of our estimate of the number of field galaxies described in section 4.2. The predicted value of A is given in Table 3 together with N_{exp} , f_f , $f_f^2 A$, and $f_c^2 \omega_{cc}$ for each subsample. Note that the contributions by field galaxies ($f_f^2 A$) to the amplitude are almost the same for the three subsamples and are negligible ($f_f^2 A < 10^{-2}$) compared with the observed amplitude at $\theta = 1^\circ$ ($\omega > 10^{-2}$, see Figure 8). Thus, we scale the observed $\omega(\theta)$ according to the values of $f_c^2 \omega_{cc}$ neglecting the term $f_f^2 \omega_{ff}$ in equation (8). If the difference in amplitude among the subsamples

with different limiting magnitudes is totally due to the contamination of field galaxies, the scaled $\omega(\theta)$ of the subsamples would agree with each other.

Figure 11 shows the $\omega(\theta)$ s of the three subsamples with different limiting magnitudes. The observed $\omega(\theta)$ of the subsample with a brighter limiting magnitude (open circles) is scaled so that the scaled $\omega(\theta)$ (filled circles) coincides with the observed $\omega(\theta)$ of the subsample with a fainter limiting magnitude if the difference between the two $\omega(\theta)$ s is totally due to the contamination of field galaxies. The $\omega(\theta)$ s of two subsamples with brighter limiting magnitudes are scaled to that of the subsample with the faintest limiting magnitude. The scaled $\omega(\theta)$ s still show a significant difference from the observed $\omega(\theta)$ of the subsample with the faintest limiting magnitude. This demonstrates that the observed strong LS is not due to the contamination of field galaxies.

6.2. Uncertainty in Morphological Classification

To evaluate the effect of the uncertainty in morphological classification, we calculate the $\omega(\theta)$ s for the lower sample which has $p = 0.3$ (see section 4.3) and the upper sample which has $p = 0.4$. Figure 12 shows W_{int} as a function of M_R^{lim} for the lower sample (dotted line) and the upper sample (dashed line) as well as the standard sample (solid line) with 1σ fluctuations estimated by BRM. The global behavior of W_{int} for both the lower and the upper samples is the same as that for the standard sample. The difference of W_{int} between the standard sample and the lower/upper sample is almost the same as or less than 1σ fluctuations of W_{int} itself over the whole magnitude range observed. We conclude that the $\omega(\theta)$ is insensitive to the errors in morphological classification.

6.3. Contamination by Stars

Our faint samples are probably contaminated by stars. We believe, however, that the fraction of mis-classified stars is negligible because the limiting magnitude of our star/galaxy separation reaches a much fainter magnitude than the limit imposed by field galaxy contamination (section 4.2), and the star counts are almost consistent with the YY92 model (Figure 3). We have also confirmed that our star sample gives $\omega(\theta) \sim 0$ over all the scales.

7. DISCUSSION

We find a strong dependence of luminosity segregation on morphology; the HCC-type galaxies show strong LS while the LCC-type galaxies show weak or no LS.

Our results are obtained for cluster galaxies distributed in an over density region on scales of $\leq 1h^{-1}$ Mpc. Almost all of the previous studies on the LS were based on cluster samples

and significant LS was found in most studies (e.g., Quintana 1979; Capelato et al. 1980; Domínguez-Tenreiro & Pozo-Sanz 1988; Salzer, Hanson, & Gavazzi 1990; Garili et al. 1992). On the other hand, among the previous studies based on the spectroscopic data of field galaxies, some claimed the significance of the LS (e.g., Davis et al. 1988; Hamilton 1988; Santiago & da Costa 1990; Maurogordato & Lachieze-Rey 1991; Loveday et al. 1995), while others cast doubt on the significance of the LS (e.g., Phillips & Shanks 1987; Tully 1988; Eder et al. 1989). In the context of our result, this disagreement in field galaxies might be due to the different morphological contents of the samples they used.

Deep photometric samples of galaxies without redshifts have been used so far to investigate the evolution of galaxy clustering with $\omega(\theta)$ (e.g., Neuschaefer, Windhorst, & Dressler 1991; Pritchet & Infante 1992; Villumsen, Freudling, & da Costa 1997). The change of amplitude of the angular two-point correlation function also reflects the evolutionary history of galaxies (Koo & Szalay 1984). In these investigations of angular two-point correlation, they assumed that the fainter galaxies in the apparent magnitude are farther from us and that the degree of galaxy clustering does not depend on luminosity. However in practice, the faint galaxies would consist of both distant galaxies and nearby dwarf galaxies. Our results suggest that the LS, that is the dependence of clustering properties on luminosity, should be taken into account when one examines the evolution of galaxy clustering. Our results also suggest that it is necessary to consider the type (HCC/LCC) mix of sample in order to investigate the LS. If the sample contains a large fraction of the HCC type, it would show significant LS. We find that the bright HCC (early type) galaxies in the Coma cluster show the LS, while the bright LCC (late type) galaxies show no LS. If this is universal for clusters of galaxies which are elliptical rich in general, a galaxy sample containing a high fraction of cluster galaxies would show the LS. Consequently, in the study of clustering evolution based on $\omega(\theta)$, it is important to take into account the fraction of cluster galaxies.

8. CONCLUSIONS

We have carried out a wide-field galaxy survey in the Coma cluster region with a mosaic CCD camera to study the clustering properties of cluster members. We have investigated the luminosity segregation (LS) quantitatively by measuring the angular two-point correlation function and radial distribution over the magnitude range of $-20 \leq M_R \leq -16$, where both giant and dwarf galaxies are included. Our analysis of the galaxy distribution based on the morphology-classified galaxy samples with the unprecedentedly deep limiting magnitude has yielded the following main results:

1. We have found that the galaxies with a high central concentration in surface brightness profile (the HCC type) have strong luminosity segregation while the galaxies with a low central concentration (the LCC type) show almost no luminosity segregation, *i.e.*, the strength of clustering of the LCC-type galaxies does not depend on luminosity.
2. We have found strong segregation in luminosity for the total sample of Coma cluster galaxies.

This is because the majority of the total sample is comprised of the HCC-type galaxies which show strong luminosity segregation.

3. Brighter HCC-type galaxies tend to more strongly concentrate near the cluster center than fainter HCC-type galaxies, while the LCC-type galaxies do not show such dependence on luminosity in the density profile.

We have shown that these results are tenable against the contamination by field galaxies and uncertainty in our method of morphological classification. Our results suggest that it would be necessary to consider this type-dependence of the LS in the study of clustering evolution with $\omega(\theta)$.

In order to see the universality of our results for clusters of galaxies in general, further studies for other clusters are necessary to investigate the luminosity and morphology dependence of galaxy distribution. It is also desired to assemble a large sample of spectroscopic data for clusters of galaxies to construct samples of confirmed cluster members.

Probably both of a primordial and an environmental effects would have influenced the clustering properties of galaxies in clusters. It is desirable to theoretically evaluate the LS due to each effect quantitatively. In addition, the observational investigation of the LS in high- z clusters would directly distinguish the effects, although morphological classification and field correction would become more difficult in such clusters.

We thank the staff of Kiso Observatory for their technical help and assistance to the development of M CCD1 and observations. We wish to thank Y. Yoshii and T. Yamagata for calculating star counts based on their model. We acknowledge the referee, A. Dressler, for valuable comments which improved the paper significantly. NK acknowledges the Fellowships of the Japan Society for the Promotion of Science for Japanese Junior Scientists. This work was supported in part by Ministry of Education, Science, and Culture through Grant in Aid (02554001, 04452016), by Toray Science Foundation, National Astronomical Observatory, and Hayakawa Foundation of the Astronomical Society of Japan.

REFERENCES

- Abraham, R.G., Valdes, F., Yee, H.K.C., & van den Bergh, S. 1994, *ApJ*, 432, 75
- Barrow, J.D., Bhavsar, S.P., & Sonoda, D.H. 1984, *MNRAS*, 210, 19
- Bahcall, N.A., & Soneira, R.M. 1983, *ApJ*, 270, 20 (BS83)
- Binggeli, B., Tammann, G.A. & Sandage, A. 1987, *AJ*, 94, 251
- Brainerd, T.G., & Villumsen, J. V. 1992, *ApJ*, 400, 398

- Briel, U.G., Henry, J.P. & Böhringer, H. 1992, *A&A*, 259, L31
- Burstein, D., & Heiles, C. 1984, *ApJS*, 54, 33
- Caldwell, N., Rose, J.A., Sharples, R.M., Ellis, R.S., & Bower, R.G., 1993, *AJ*, 106, 473
- Capelato, H.G., Gerbal, D., Mathez, G., Mazure, A., Salvadole-Sole, E., & Sol, H. 1980, *ApJ*, 241, 521
- Davis, M. & Geller, M.J. 1976, *ApJ*, 208, 13
- Davis, M., Efstathiou, G., Frenk, C.S., White, S.D.M. 1985, *ApJ*, 292, 371
- Davis, M., Meiksin, A., Strauss, A., Nicolaci da Costa, L., & Yahil, A. 1988, *ApJ*, 333, L9
- de Lapparent, V., Geller, M.J., & Huchra, J.P. 1988, *ApJ*, 332, 44
- Diaconis, P., & Efron, B. 1983, *Sci.Am.*, 1993, 96
- Doi, M., Fukugita, M., & Okamura, S. 1993, *MNRAS*, 264, 832
- Doi, M., Fukugita, M., & Okamura, S. 1995, *ApJS*, 97, 59
- Domínguez-Tenreiro, R., & Pozo-Sanz, R.D. 1988, *ApJ*, 324, 677
- Dressler, A. 1980a, *ApJS*, 42, 565
- Dressler, A. 1980b, *ApJ*, 236, 351
- Eder, J.A., Schombert, J.M., Dekel, A., & Oemler, A.Jr. 1989, *ApJ*, 340, 29
- Efstathiou, G., Ellis, R.S., & Peterson, B.A. 1988, *MNRAS*, 232, 431
- Einasto, M. 1991, *MNRAS*, 250, 802
- Ferguson, H.C., & Bingelli, B. 1994, *A&A Rev.*, 6, 67
- Ferguson, H.C., & Sandage, A., 1989, *ApJ*, 346, L53
- Forbes, D., & Dawson, P.C. 1986, *PASP*, 98, 102
- Garili, B., Bottini, D., Maccagni, D., Vettolani, G., & Maccacaro, T. 1992, *AJ*, 104, 1290
- Groth, E.J. 1986, *AJ*, 91, 1244
- Groth, E.J., & Peebles, P.J.E. 1977, *ApJ*, 217, 385
- Hamilton, A.J.S. 1988, *ApJ*, 331, L59
- Kaiser, N. 1984, *ApJ*, 284, L9

- Kashikawa, N., Sekiguchi, M., Yagi, M., Yasuda, N., Shimasaku, K., Doi, M., & Okamura, S., 1995a, in "Scientific and Engineering Frontiers for 8-10m Telescopes", M. Iye and T. Nishimura eds., Universal Academy Press, p.105
- Kashikawa, N., Shimasaku, K., Yagi, M., Yasuda, N., Doi, M., Okamura, S., & Sekiguchi, M., 1995b, *ApJ*, 452, L99
- Koo, D.C., & Szalay, A.S. 1984, *ApJ*, 282, 390
- Loveday, J., Maddox, S.J., Efstathiou, G., & Peterson, B.A. 1995, *ApJ*, 442, 457
- Lasker, B.M., Sturch, C.R., McLean, B.J., Russell, J.L., Jenker, H., & Shara, M.M., *AJ*, 99, 2019
- Maurogordato, S. & Lachize-Rey, M. 1991, *ApJ*, 369, 30
- Mo, H.J., Jing, Y.P., & Börner, G. 1992, *ApJ*, 392, 452 Dressler, A., & Oemler, Jr.A. 1996, *Nature*, 379, 613
- Neuschaefer, L.W., Windhorst, R.A., & Dressler, A. 1991, *ApJ*, 382, 32
- Oemler, A.Jr. 1974, *ApJ*, 194, 1
- Okamura, S., Kodaira, K., & Watanabe, M. 1984, *ApJ*, 280, 7
- Okamura, S., Doi, M., Kashikawa, N., Kawasaki, W., Komiyama, Y., Sekiguchi, M., Shimasaku, K., Yagi, M., & Yasuda, N. 1996, *Proc. IAU Symposium No. 179: "New Horizons from Multi-Wavelength Sky Surveys"*, in press
- Peebles, P.J.E. 1980, in *The Large-Scale Structure of the Universe* (Princeton: Princeton Univ. Press)
- Phillips, S. & Shanks, T. 1987, *MNRAS*, 229, 621
- Pritchett, C.J., & Infante, L. 1992, *ApJ*, 399, L35
- Quintana, H. 1979, *AJ*, 84, 15
- Salzer, J.J., Hanson, M.M., & Gavazzi, G. 1990, *ApJ*, 353, 39
- Santiago, B.X., & da Costa, L.N. 1990, *ApJ*, 362, 386
- Sekiguchi, M., Iwashita, H., Doi, M., Kashikawa, N., & Okamura, S. 1992, *PASP*, 104, 744
- Shanks, T., Fong, R., Ellis, R.S., & MacGillivray, H.T. 1980, *MNRAS*, 192, 209
- Thompson, L.A. 1993, *AJ*, 106, 2197
- Tully, R.B. 1988, *AJ*, 96, 173

- Valls-Gebaud, D., Alimi, J., & Blanchard, A. 1989, *Nature*, 341, 215
- van den Bergh, S. 1986, *AJ*, 91, 271
- Villumsen, J., Freudling, W., & da Costa, L. 1997, *ApJ*, 481, 578
- White, S.D.M., Davis, M., Efstathiou, G., & Frenk, C.S. 1987, *Nature*, 330, 451
- Yagi, M. et al. 1998, in preparation
- Yamagata, T. & Yoshii, Y. 1992, *AJ*, 103, 117 (YY92)
- Yoshii, Y. & Takahara, F. 1988, *ApJ*, 326, 1
- Yoshii, Y. 1993, *ApJ*, 403, 552
- Zabludoff, A.I., Geller, M.J., Huchra, J.P. 1993, *AJ*, 106, 1273

Fig. 1.— Configuration of CCDs of M CCD1. Each CCD has 1000×1018 effective pixels. The angular scale is shown when the camera is mounted on the prime focus of Kiso Schmidt. North is up and west is to the left.

Fig. 2.— Plot of $\log(I_{peak}/N_{pix})$ vs. R -band apparent magnitude for the Coma cluster field. Stars form a well-defined continuous sequence running from top-left to middle-right in the panel. Galaxies are distributed widely below the star sequence. The solid line is the boundary we adopt for star/galaxy discrimination.

Fig. 3.— Comparison of our star counts with YY92 model and BS83 model. Filled circles indicates the observed star counts based on the boundary line we define. The solid line is for the prediction of the model by Yamagata & Yoshii (1992), and the dotted line is for that by Bahcall & Soneira (1983).

Fig. 4.— $m_R - C_{in}$ plot of Dressler’s sample. The pair of the solid lines and the pair of the dotted lines correspond to the loci of the HCC-type model galaxies and the LCC-type model galaxies, respectively. In the respective pairs of lines, the upper and lower ones correspond to the models with the minimum SB and the maximum SB respectively. These lines are for the same seeing size and the same threshold level as for the observed data. Filled circles are galaxies classified as E or S0 in Dressler (1980a) and open circles are those classified as S. Because of wide SB range, the sample is divided into two panels in regard to SB .

Fig. 5.— Completeness of the HCC types (solid line) and the LCC types (dotted line) as a function of p . We define the ‘standard’ sample with $p = 0.35$ where the two curves intersect with each other.

Fig. 6.— Magnitude versus C_{in} plot of the standard ($p = 0.35$) sample. Filled circles are galaxies classified as the HCC type, and open circles are those classified as the LCC type.

Fig. 7.— Sky distribution of galaxies of (a) the total sample, (b) the HCC sample, and (c) the LCC sample. The size of a circle is proportional to the luminosity of the galaxy.

Fig. 8.— The $\omega(\theta)$ s of subsamples with different luminosity extracted from (a) the total sample, the (b) the HCC sample, and (c) the LCC sample. The solid line denotes the bright sample, the dotted line denotes the intermediate sample, and the dashed line denotes the faint sample.

Fig. 9.— W_{int} as a function of limiting magnitude M_R^{lim} . The solid line represents the HCC sample and the dotted line represents the LCC sample. The dashed line denotes the faintest magnitude limited by the contamination of field galaxy. The error bars denote the fluctuations of W_{int} estimated by BRM.

Fig. 10.— Surface number density (/sqdeg) of galaxies in the subsamples with different luminosities and morphologies as a function of the distance from the cluster center. The left panels show the surface number density for the HCC sample and the right panels show for the LCC sample. From

top to bottom: the bright sample, the intermediate sample, and the faint sample.

Fig. 11.— Scaling test for the total sample. The sample with brighter limiting magnitude (filled circle and filled square) is scaled to that with fainter limiting magnitude (filled triangle) according to the values given in Table 3 (see the text for details). The open symbols denote the $\omega(\theta)$ s for subsample with brighter magnitude before scaling.

Fig. 12.— W_{int} as a function of limiting magnitude when the lower and upper samples are used. The solid line represents the standard sample (same as Figure 9) with one sigma fluctuations of W_{int} estimated by BRM. The dotted line represents lower sample and the dashed line upper sample.

Table 1. The number of galaxies of our Coma cluster and SA57 samples and the expected contamination rate of field galaxies

m_R^{lim}	M_R^{lim}	N_{Coma}^a	N_{SA57}^b	contamination rate
15.73	–18.5	243	68.5	0.28
16.23	–18.0	338	79.8	0.24
16.73	–17.5	499	125.	0.25
17.23	–17.0	747	228.	0.31
17.73	–16.5	1172	548.	0.47
18.23	–16.0	1805	890.	0.49

^aNumber of galaxies in Coma sample (/5.25sqdeg)

^bNumber of field galaxies(/5.25sqdeg) estimated from SA57 sample

Table 2. Fitting parameters of $\omega(\theta)$ for total sample and subsamples from different morphology and different luminosity

morph.type	M_R	N	γ	$\delta\gamma$	A_ω	δA_ω	W_{int}	δW_{int}
total	– –18.0	338	–0.430	0.090	0.377	0.066	0.483	0.064
	–18.0 – –17.0	409	–0.379	0.250	0.113	0.048	0.139	0.036
	–17.0 – –16.0	1058	–0.404	0.251	0.029	0.015	0.036	0.013
HCC	– –18.0	215	–0.434	0.106	0.499	0.113	0.642	0.106
	–18.0 – –17.0	281	–0.377	0.264	0.126	0.052	0.154	0.045
	–17.0 – –16.0	817	–0.711	0.412	0.014	0.012	0.024	0.013
LCC	– –18.0	123	–0.690	0.291	0.156	0.078	0.257	0.092
	–18.0 – –17.0	128	–0.661	0.393	0.079	0.051	0.125	0.058
	–17.0 – –16.0	241	–0.396	0.544	0.057	0.027	0.071	0.023

Table 3. Parameters for scaling test

M_R^{lim}	N_{exp}	A	f_f	$f_f^2 A$	$f_c^2 \omega_{cc}$
–18.0	15.2	9.02×10^{-2}	0.24	5.20×10^{-3}	$0.58\omega_{cc}$
–17.0	43.4	5.22×10^{-2}	0.31	5.02×10^{-3}	$0.48\omega_{cc}$
–16.0	169.5	3.18×10^{-2}	0.49	7.64×10^{-3}	$0.26\omega_{cc}$

CCD Geometry of M CCD1

1pix=0."75

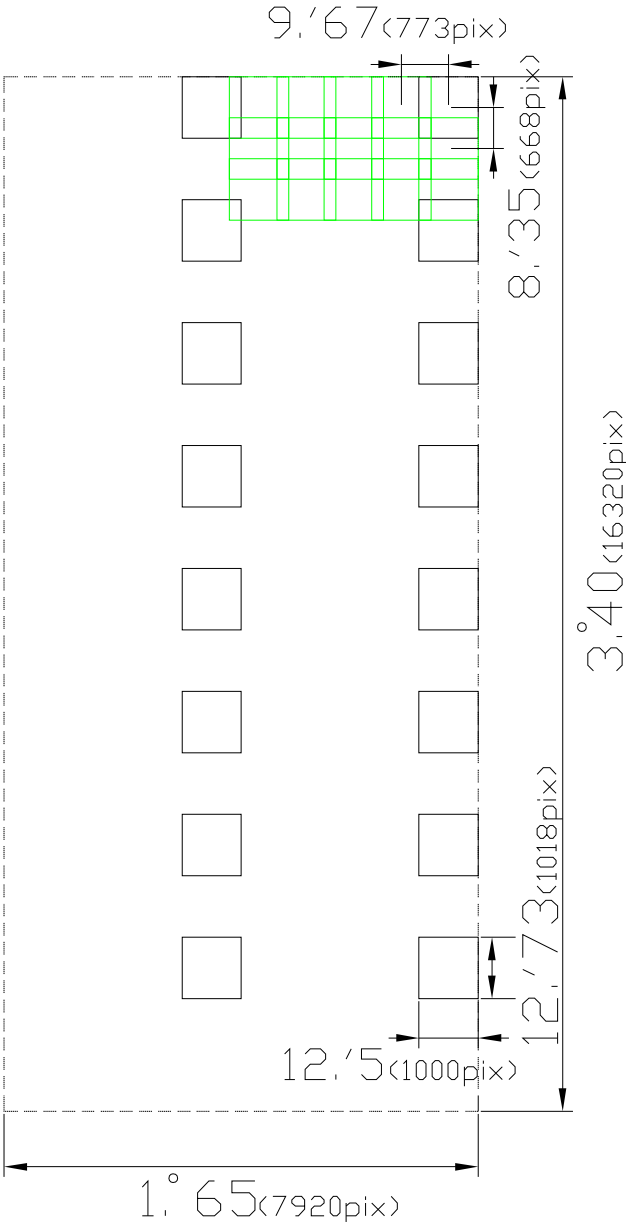


Fig. 1

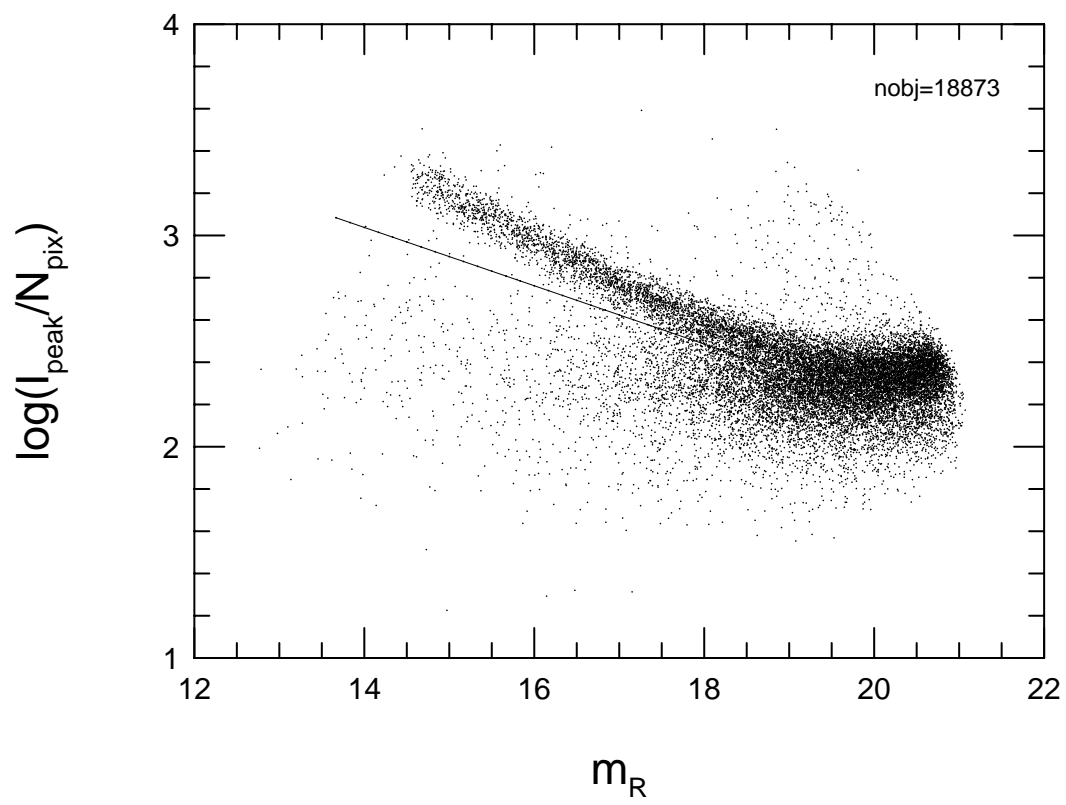


Fig. 2

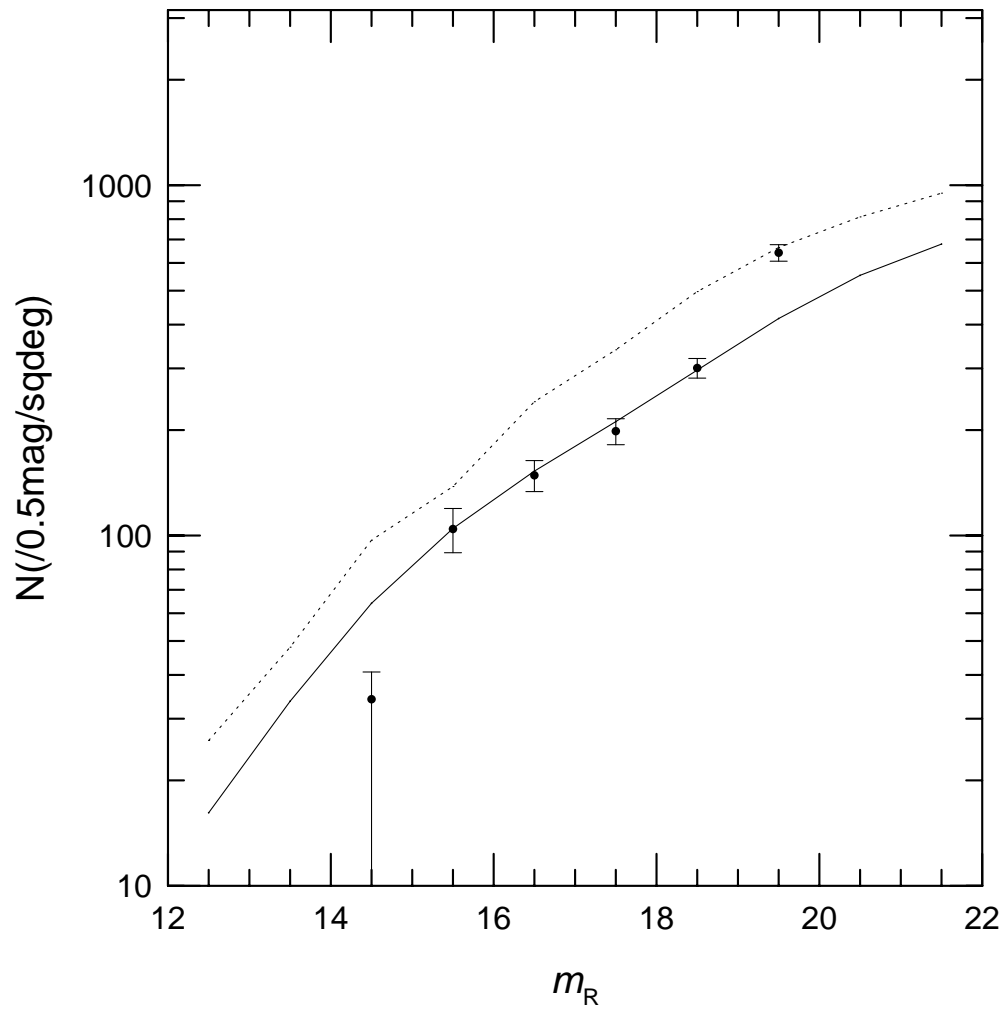


Fig. 3

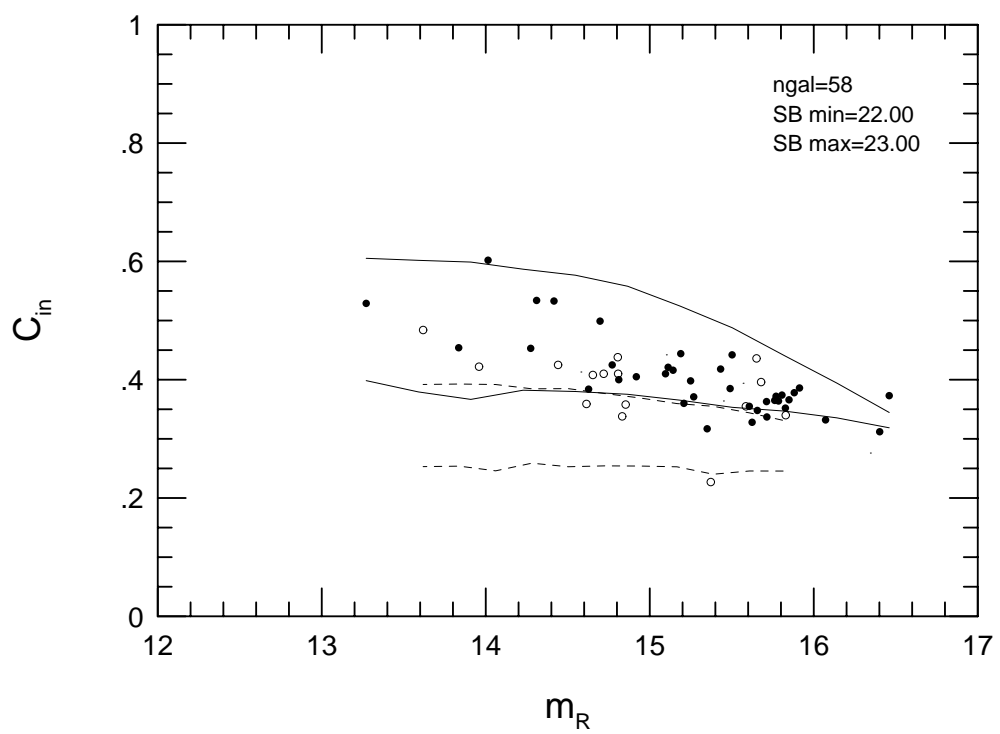
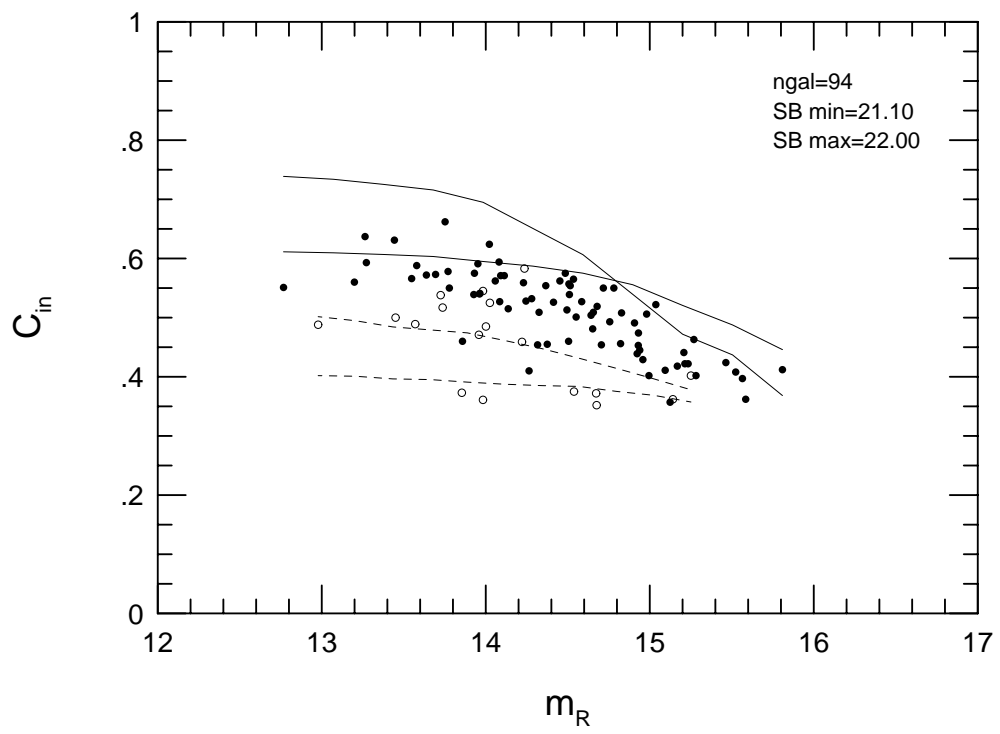


Fig. 4

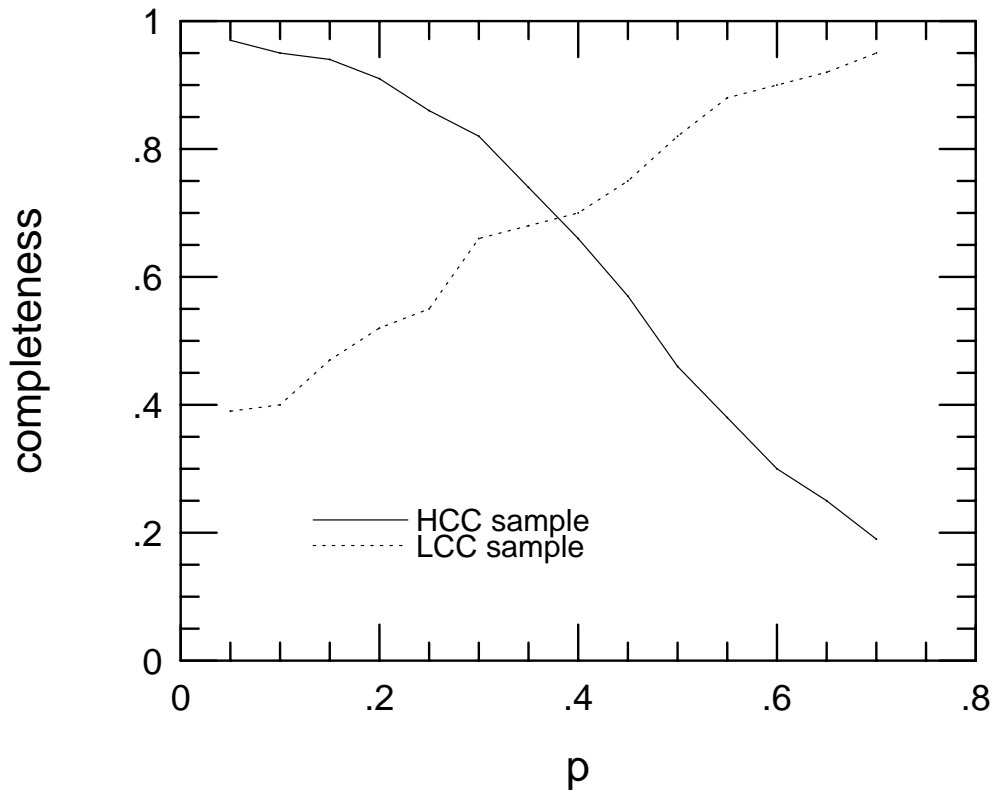


Fig. 5

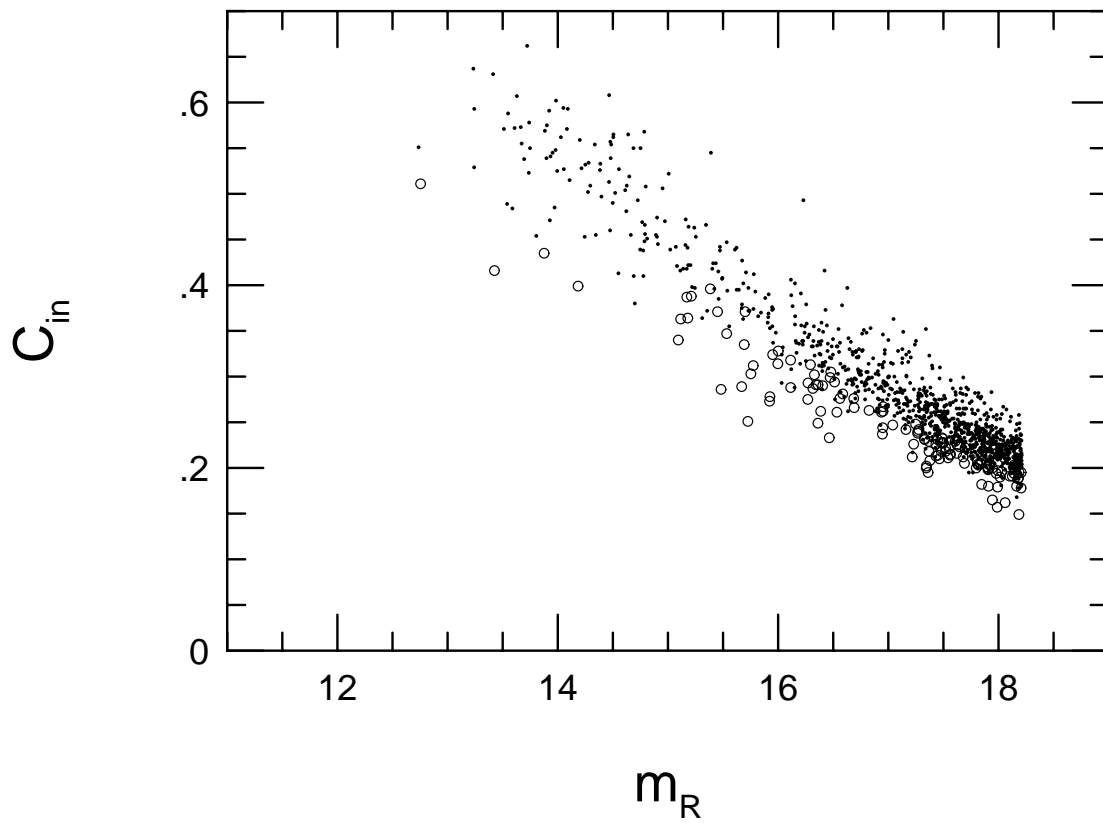
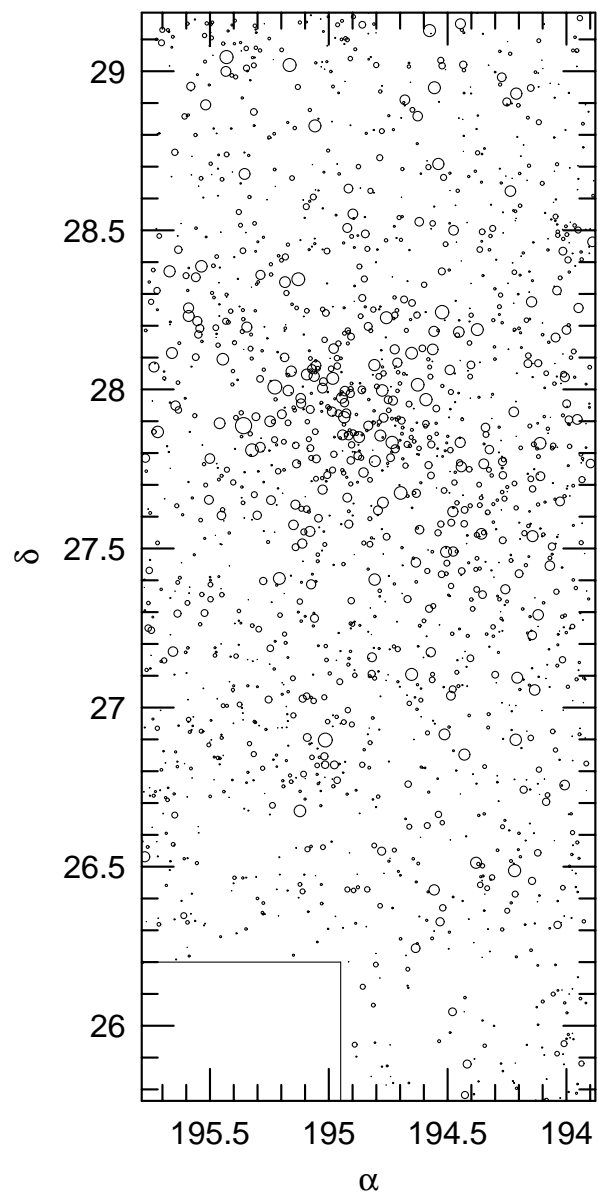
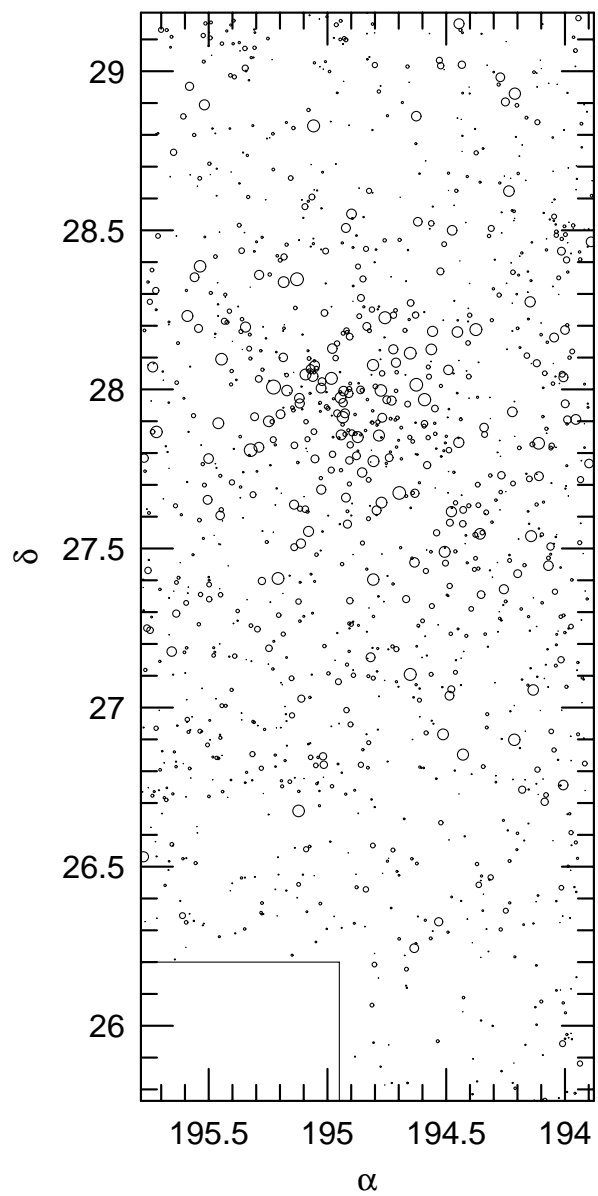


Fig. 6

(a) total sample



(b) HCC sample



(c) LCC sample

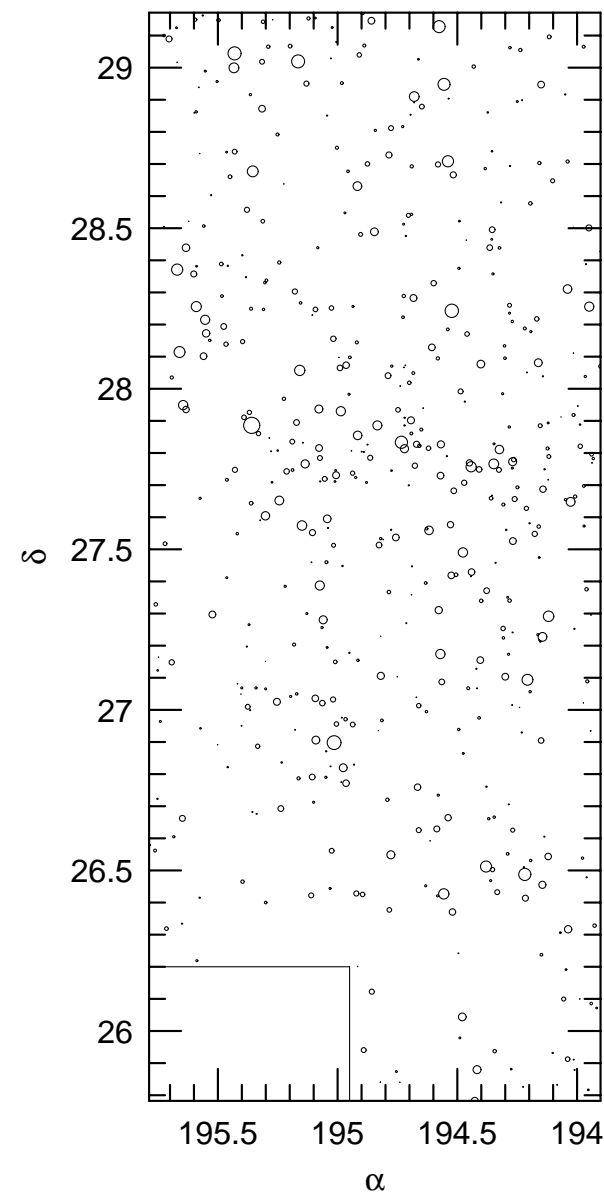


Fig. 7

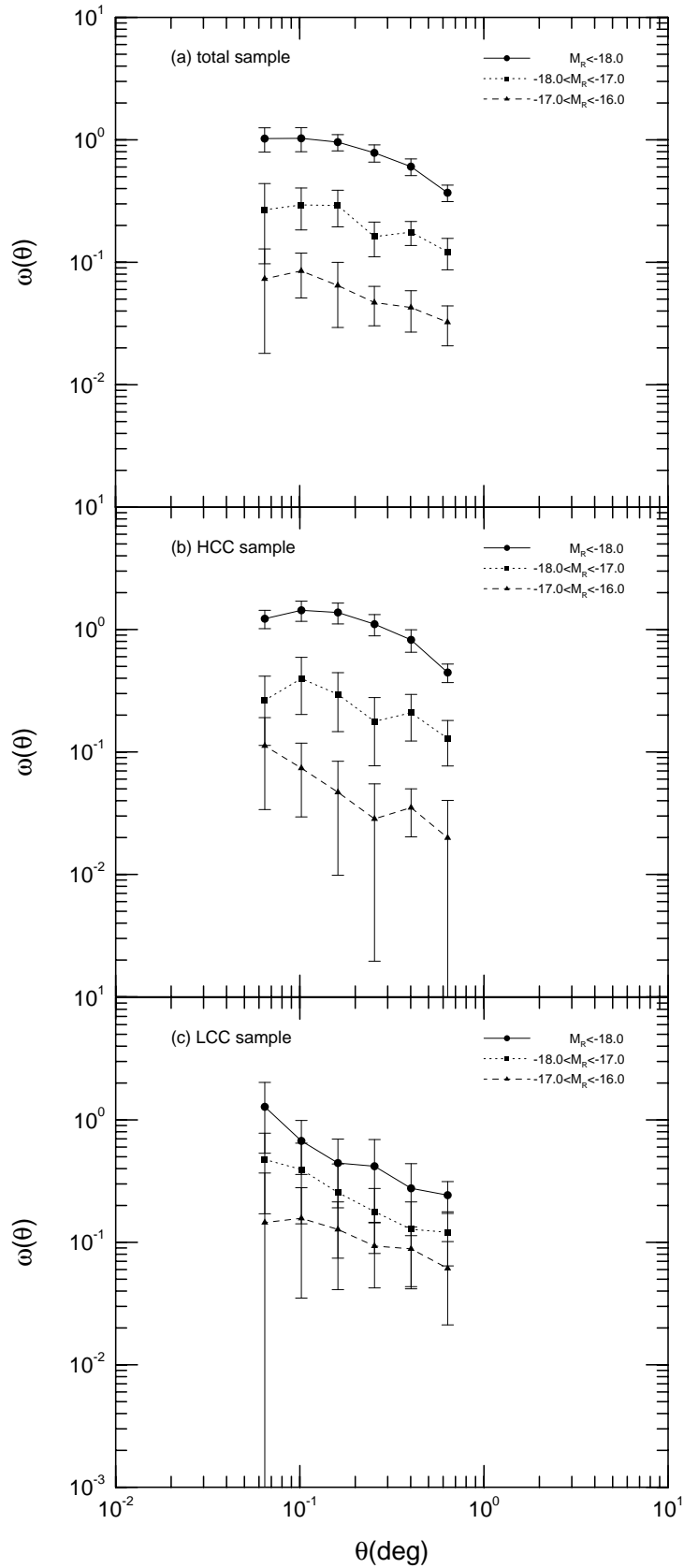


Fig. 8

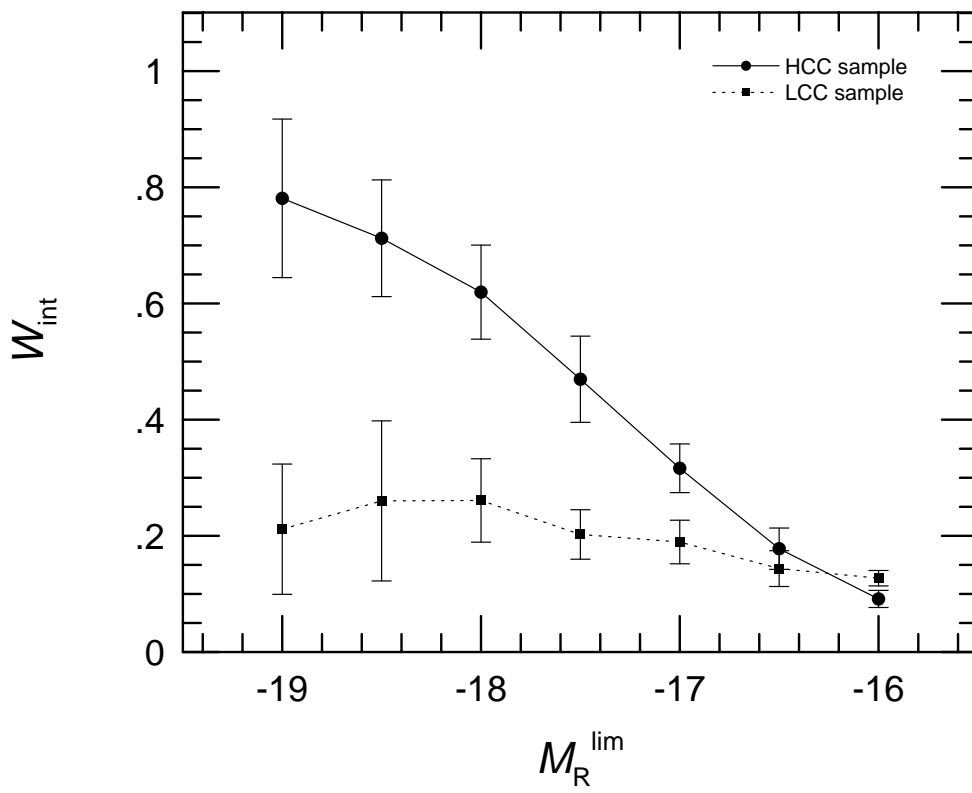


Fig. 9

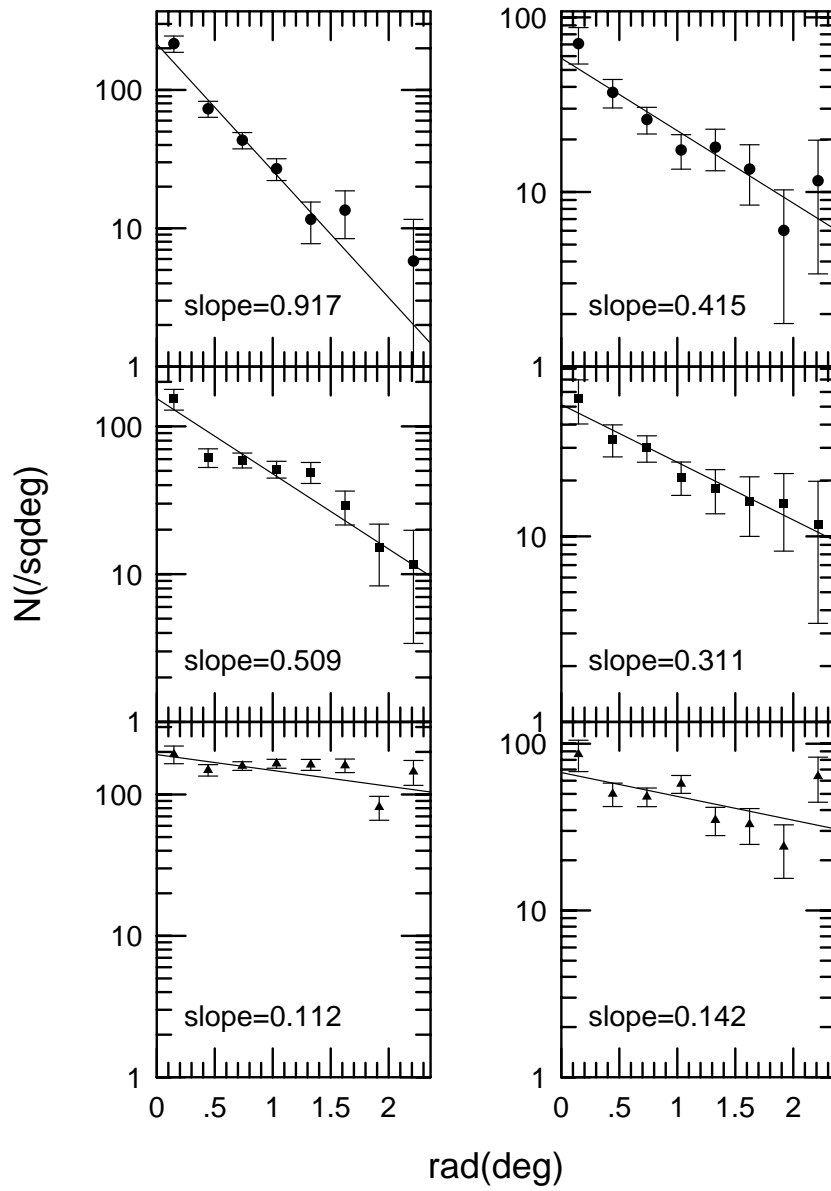


Fig. 10

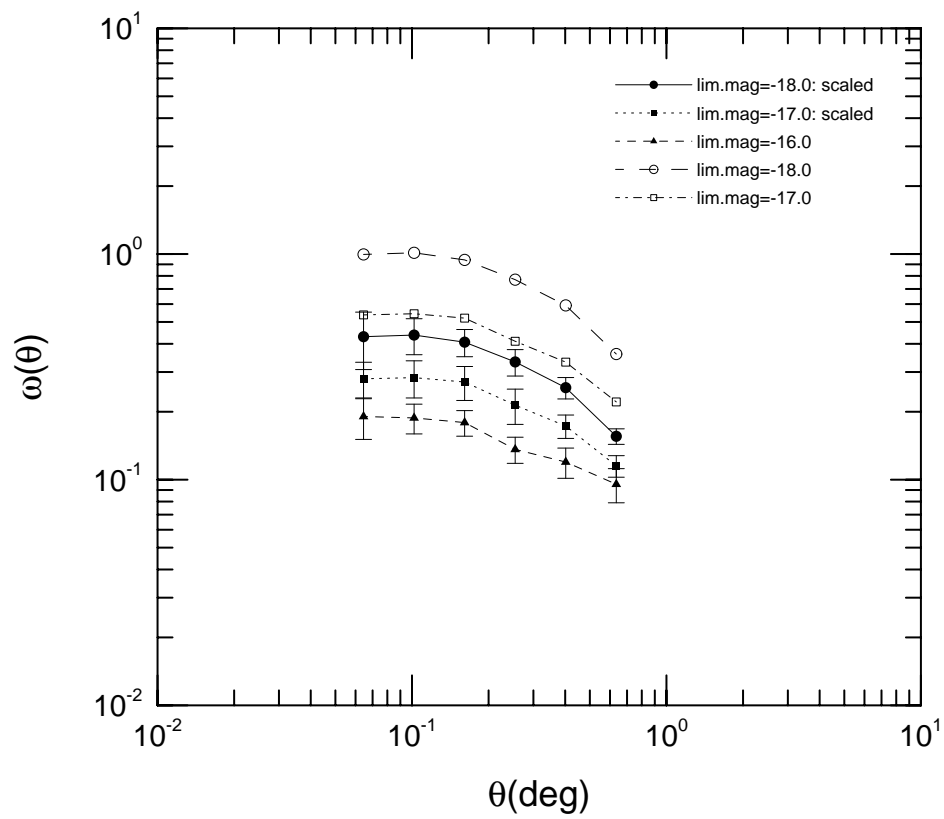


Fig. 11

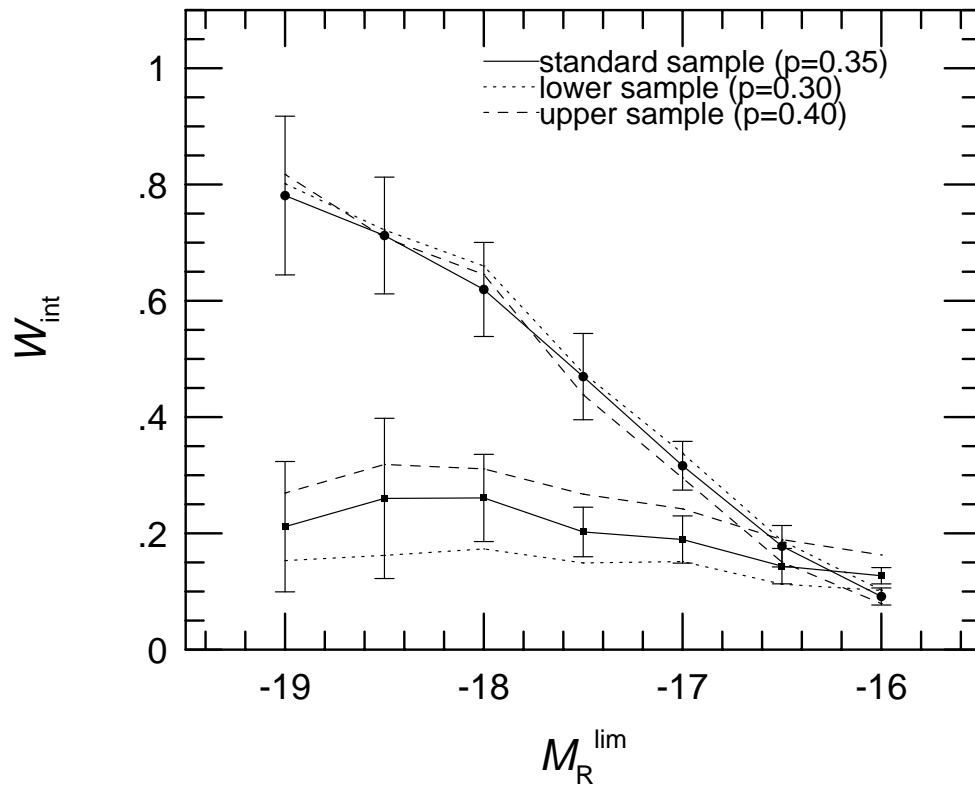


Fig. 12